

Article

Synchronous Resonant Control Technique to Address Power Grid Instability Problems Due to High Renewables Penetration

Majid Mehrasa ¹, Edris Pouresmaeil ^{2,*} , Bahram Pournazarian ², Amir Sepehr ² ,
Mousa Marzband ³  and João P. S. Catalão ^{1,4,5}

¹ C-MAST, University of Beira Interior, 6201-001 Covilhã, Portugal; m.majidmehrassa@gmail.com (M.M.); catalao@ubi.pt (J.P.S.C.)

² Department of Electrical Engineering and Automation, Aalto University, 02150 Espoo, Finland; bahram.poomazaryan@gmail.com (B.P.); a.sepehr@alumni.ut.ac.ir (A.S.)

³ Faculty of Engineering and Environment, Department of Physics and Electrical Engineering, Northumbria University Newcastle, Newcastle NE1 8ST, UK; mousa.marzband@northumbria.ac.uk

⁴ INESC TEC and the Faculty of Engineering, University of Porto, 4200-465 Porto, Portugal

⁵ INESC-ID, Instituto Superior Técnico, University of Lisbon, 1049-001 Lisbon, Portugal

* Correspondence: edris.pouresmaeil@aalto.fi; Tel.: +358-505-984-479

Received: 28 August 2018; Accepted: 10 September 2018; Published: 17 September 2018



Abstract: This paper presents a synchronous resonant control strategy based on the inherent characteristics of permanent magnet synchronous generators (PMSG) for the control of power converters to provide stable operating conditions for the power grid under high penetration of renewable energy resources (RERs). The proposed control technique is based on the small signal linearization of a dynamic model with grid specifications, load-current-based voltages, and power converter currents. A combination of the linearized dynamic model with the PMSG swing equation and resonant controller leads to a control technique with synchronous features and appropriate inertia for the control of converter-based power generators. As the main contribution of this work, an extra functionality is proposed in the control loop of the proposed model to solve the inherent inconveniences of conventional synchronous generators. Also, a comprehensive collaboration between interfaced converter specifications and PMSG features is achieved as another contribution of the proposed control technique, and this can guarantee accurate performance under various conditions. A current perturbation curve is introduced to assess the variations of the grid frequency and voltage magnitude under operation of the interfaced converters controlled by the proposed control technique. Moreover, by taking into account the load-based voltages, the effects of the current perturbation components are investigated. The proposed model is simulated in MATLAB/Simulink environment to verify the high performance of the proposed control technique over the other existing control methods.

Keywords: renewable energies; synchronous resonant control strategy; current perturbation curve; grid voltage; frequency regulation

1. Introduction

Using the generation systems in the microgrid structures leads to a consideration of issues related to designing nonlinear controllers, such as passivity/sliding [1], power management [2,3], analysis and detection of failure [4], and so on. Among various applications of power converters in the power grid, e.g., active power filters (APF) [5], distributed generation (DG) technologies [6], microgrids [7], and so on [8,9], the issues resulting from high penetration of renewable energy resources (RERs) into

the power grid have attracted significant attention in order to solve the problems associated with the stability of the power grid [10,11]. This is always an issue with the renewable energy resources, including wind energy [12], photovoltaic systems [13,14], maximum solar-based power [15] and so on. Power converters are normally considered to be the heart of the interfacing system between RERs and the power grid, and the lack of inertia in these converter-based power generators, in addition to their odd transient dynamics behavior, increases their negative impacts on power grid stability, which is the opposite of the operation of synchronous generators. To deal with this issue, electrical engineering scientists have proposed emulation of the behavior of permanent magnet synchronous generators (PMSG) by power converters [16,17]. Using this assumption, converter-based generators work based on the inherent characteristics of PMSG. Many works in the literature have discussed renewable energy resources previously, along with several important topics related to reactive power management [18], dynamic operation and control [19], and the design of intelligent controllers [20–22]. Moreover, the problems regarding faults [23,24], coordinated control strategies [25], and the use of energy storage systems [26] have been investigated, as well.

Several studies have been reported in the literature regarding control of power converters under large-scale integration of RERs into the power grid [27–39]. In [27], a virtual synchronous generator (VSG) was proposed to make an emulation strategy [28,29] for the improvement of the swing equation damping power. The proposed strategy does not require a phase-locked-loop (PLL) and can remove the effects of the droop coefficient due to the traditional constant damping factor. The transient stability of a multi-VSG microgrid was evaluated in [30] by defining the generator's voltage angle deviations, along with the angle of the center of inertia. In addition, by considering an effective inertia for the VSG-based microgrid, decreasing oscillations and improving transient stability against the large disturbances can be quickly accomplished. The adaptive virtual inertia value introduced in [31], which is able to provide a large inertia while the frequency deviation is high, provides a low inertia operation to recover the frequency. A distributed voltage control strategy was proposed in [32] for photovoltaic power plant application to reduce the high ramp-rate disturbances. In [33], the basic trends of the VSG were investigated based on the features of the synchronous generator (SG), the main advantages and disadvantages of which were studied in detail. It was also found that converter features can lead to an improved VSG, leading to better responses and functionalities in comparison with the traditional generators. By emulation of the behavior of SG based on its well-known frequency and voltage droop mechanisms, the synchronous operation of converters was realized in [34]. Such emulation causes the converters to have a synchronized behavior in parallel connections under both grid-connected and islanded microgrid operating modes. By employing the PLL dynamic of the voltage source converters (VSC), an equivalent SG model has been proposed in [35] for the current-controller-based VSCs. An emulation-based control method of SG consisting of both inner and outer control loops was proposed for a VSC-High Voltage Direct Current (HVDC) in [36], for which the reference frequency value was obtained by an inertia element and scheduled power modulation was utilized as a secondary frequency regulation. A combined model consisting of a virtual inertia emulator and a hybrid battery-supercapacitor-based energy storage system was proposed in [37]. The proposed model could simultaneously increase the stability of microgrids and reduce the short-term power oscillations by enhancing the inertial response using the kinetic inertia emulation of the SG. The use of SG emulation was considered in [38,39] to address the frequency control issues.

In this paper, a synchronous resonant control technique is proposed based on the inherent features of PMSG to deal with the stability issues of the power grid under large-scale integration of RERs. The rest of paper is organized as follows: in Section 2, a dynamic model based on the grid parameters, load-based voltages, and interfaced converter currents is achieved. Then, the proposed control technique is presented by applying small-signal linearization to the proposed dynamic model, the PMSG equations, and the apparent power relationship of the interfaced converter. The dynamics model of the interfaced converter and PMSG behaviors are coordinated through a comprehensive

detailed relationship, which is considered to be another contribution of this paper. Section 3 presents the effects of various components of the proposed control technique on the injected currents from the interfaced converter to the grid. Section 4 investigates to what extent the variations of grid frequency and voltage magnitude can impact the current errors injected by power converters. In Section 5, the impacts of the considered currents errors variations on the load-based voltages are assessed. Finally, simulation results are presented in Section 6 and the conclusion is drawn in Section 7.

2. The Proposed Control Technique

The main structure of the proposed synchronous active proportional-integral-resonance controller (SAPIRC) is presented in this section. According to Figure 1, the proposed model is comprised of the power grid, the grid-connected load, the RERs, and the interfaced converters. Both connection and disconnection of the large-scale RERs will be implemented in this paper to assess the ability of the proposed control technique to guarantee stable operating conditions for the power grid. To achieve this, a dynamic model will be presented, and subsequently, a control strategy will be proposed based on inherent features of PMSG.

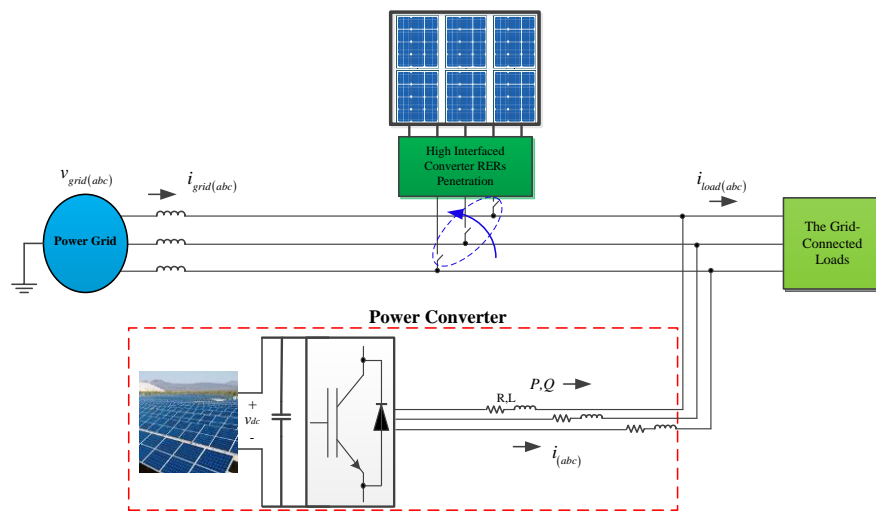


Figure 1. General structure of the proposed model.

A. The Proposed Dynamic Model Analysis

To draw an appropriate plan to control the interfaced converters between RERs and the power grid, a dynamic analytical model of Figure 1 is developed. Bearing in mind this assumption, the dynamic model based on the power grid specification and d - q voltages at the point of common coupling (PCC) can be achieved as [6]:

$$L_g \frac{di_{gd}}{dt} + R_g i_{gd} - \omega L_g i_{gq} = v_{gd} - v_d \quad (1)$$

$$L_g \frac{di_{gq}}{dt} + R_g i_{gq} + \omega L_g i_{gd} = v_{gq} - v_q \quad (2)$$

where the voltage $v_{gdq} - v_{dq}$ shows the magnitude of the grid voltage variation, which should be equal to zero under ideal conditions. As can be seen in Figure 1, the relationship between the grid-connected load, the power grid, and the interfaced converter currents in the d - q reference frame can be expressed as:

$$i_{ldq} = i_{gdq} + i_{dq} \quad (3)$$

By substituting (3) into both (1) and (2), the dynamic equation based on the currents of the interfaced converter can be achieved as:

$$\begin{aligned} L_g \frac{di_d}{dt} + R_g i_d - \omega L_g i_q + v_{gd} - v_d &= v_1 (i_{ld}, i_{lq}) \\ L_g \frac{di_q}{dt} + R_g i_q + \omega L_g i_d + v_{gq} - v_q &= v_2 (i_{ld}, i_{lq}) \end{aligned} \quad (4)$$

The voltages v_1 and v_2 are dependent on the grid-connected load, which can be obtained as:

$$\begin{aligned} v_1 (i_{ld}, i_{lq}) &= R_g i_{ld} - \omega L_g i_{lq} \\ v_2 (i_{ld}, i_{lq}) &= R_g i_{lq} + \omega L_g i_{ld} \end{aligned} \quad (5)$$

Also, as can be understood from (5), the voltages v_1 and v_2 will be changed by the grid frequency and impedance variation. This feature results in the proposed dynamic model in (4), including all the specifications of grid, load, and interfaced converter.

B. The Proposed SAPIRC-Based Controller

In this sub-section, the proposed control technique is presented based on Equation (4) and the inherent characteristics of the PMSG. By applying small signal linearization to (4), the linearized Equations (6) and (7) can be derived as:

$$(L_g s + R_g) \Delta i_d - L_g i_q^* \Delta \omega - \omega^* L_g \Delta i_q + \Delta v_{gd} - \Delta v_d = \Delta v_1 (i_{ld}, i_{lq}) \quad (6)$$

$$(L_g s + R_g) \Delta i_q + L_g i_d^* \Delta \omega + \omega^* L_g \Delta i_d + \Delta v_{gq} - \Delta v_q = \Delta v_2 (i_{ld}, i_{lq}) \quad (7)$$

With an acceptable approximation $\Delta v_q = 0$, it can be considered that $P = v_d i_d$. Thus, the small signal linearization of the active power P can be written as:

$$\Delta i_d = \frac{\Delta P v_d^* - \Delta v_d P^*}{v_d^{*2}} \quad (8)$$

To achieve the perturbation component of current of the SAPIRC-based converter on the d -axis, the Δv_d and Δi_q are firstly derived from (6) and (7), respectively, and then the results will be substituted into (8). Thus, (9) can be expressed as:

$$\begin{aligned} \Delta i_d &= \Delta P \frac{(L_g s + R_g) v_d^*}{\Delta} + \left(\frac{(L_g i_q^* P^*) (L_g s + R_g) - L_g i_d^* \omega^* L_g P^*}{\Delta} \right) \Delta \omega \\ &- \left(\frac{\omega^* L_g P^*}{\Delta} \right) \Delta v_{gq} + \left(\frac{\omega^* L_g P^*}{\Delta} \right) \Delta v_2 (i_{ld}, i_{lq}) - \frac{(P^*) (L_g s + R_g)}{\Delta} \Delta v_{gd} + \frac{(P^*) (L_g s + R_g)}{\Delta} \Delta v_1 (i_{ld}, i_{lq}) \end{aligned} \quad (9)$$

where

$$\Delta = \left(P^* L_g^2 s^2 + \left(2R_g L_g P^* + v_d^{*2} L_g \right) s + \left(v_d^{*2} R_g + P^* R_g^2 + \omega^{*2} L_g^2 P^* \right) \right)$$

On the other hand, by combining the relationships between $P = v_d i_d$ and $Q = -v_d i_q$, the following equation can be expressed as:

$$P i_q = -Q i_d \quad (10)$$

To make a relationship between Δi_q and the perturbation components of active and reactive powers of the SAPIRC-based converter, small signal linearization should be applied to (10), which leads to:

$$\Delta i_q = \left(-\Delta Q i_d^* - \Delta P i_q^* - Q^* \Delta i_d \right) / P^* \quad (11)$$

As can be seen, the perturbation part of q -component of the SAPIRC-based converter current is dependent on all the perturbation parts of Δi_d , ΔP and ΔQ . The relationship between the electrical and mechanical parts of a PMSG can be stated as the following swing equation [29]:

$$\frac{1}{2}J \frac{d(\omega^2)}{dt} = P_m - P \tag{12}$$

Applying small signal linearization to (12) will lead to:

$$\Delta P = \Delta P_m - (\omega^* J s + (P_m^* - P^*)/\omega^*)(\Delta \omega) \tag{13}$$

As is known, the relationship between the apparent power and both active and reactive powers can be written as $P^2 + Q^2 = S^2$. When considering a constant value for the apparent power of the SAPIRC-based converter, the following equation can be achieved for the reactive power perturbation part using the stated relation and (13) as:

$$\Delta Q = \frac{P^*}{Q^*} (\omega^* J s + (P_m^* - P^*)/\omega^*)(\Delta \omega) - \frac{P^*}{Q^*} \Delta P_m \tag{14}$$

By substituting (13) into (9), along with some simplifications, the perturbation component of the d component of the interfaced converter based on PMSG features can be expressed as:

$$\Delta i_d = G_{md} \Delta P_m + G_{pd} \Delta P - G_{gqd} \Delta v_{gq} + G_{v2d} \Delta v_2 - G_{gdd} \Delta v_{gd} + G_{v1d} \Delta v_1 \tag{15}$$

where various transfer functions of (15) are as follows:

$$\begin{aligned} G_{md} &= \frac{[P^* L_g^2 i_q^* s + (R_g P^* L_g i_q^* - P^* \omega^* L_g^2 i_d^*)]}{\Delta_d} \\ G_{pd} &= \frac{\left(J \omega^* v_d^* L_g s^2 + \left[((P_m^* - P^*)/\omega^*) v_d^* L_g + J \omega^* v_d^* R_g - P^* L_g^2 i_q^* \right] s \right)}{\Delta_d} \\ &\quad + \frac{\left[((P_m^* - P^*)/\omega^*) v_d^* R_g - R_g P^* L_g i_q^* + P^* \omega^* L_g^2 i_d^* \right]}{\Delta_d} \\ G_{gqd} &= \frac{(J P^* \omega^{*2} L_g s + (P_m^* - P^*) P^* L_g)}{\Delta_d} \\ G_{v2d} &= \frac{(J P^* \omega^{*2} L_g s + (P_m^* - P^*) P^* L_g)}{\Delta_d} \\ G_{gdd} &= \frac{(J \omega^* L_g P^* s^2 + [((P_m^* - P^*)/\omega^*) L_g P^* + J \omega^* R_g P^*] s + ((P_m^* - P^*)/\omega^*) R_g P^*)}{\Delta_d} \\ G_{v1d} &= \frac{(J \omega^* L_g P^* s^2 + [((P_m^* - P^*)/\omega^*) L_g P^* + J \omega^* R_g P^*] s + ((P_m^* - P^*)/\omega^*) R_g P^*)}{\Delta_d} \\ \Delta_d &= \left(\begin{aligned} &P^* L_g^2 J \omega^* s^3 + \left[(v_d^{*2} L_g + 2 P^* R_g L_g) J \omega^* + P^* L_g^2 ((P_m^* - P^*)/\omega^*) \right] s^2 \\ &+ \left[(R_g^2 P^* + P^* \omega^{*2} L_g^2 + v_d^{*2} R_g) J \omega^* + (v_d^{*2} L_g + 2 P^* R_g L_g) ((P_m^* - P^*)/\omega^*) \right] s \\ &+ (R_g^2 P^* + P^* \omega^{*2} L_g^2 + v_d^{*2} R_g) ((P_m^* - P^*)/\omega^*) \end{aligned} \right) \end{aligned}$$

Also, by substituting (13)–(15) into (11), the relationship between Δi_q based on the proposed model and the PMSG specifications can be expressed as:

$$\Delta i_q = -G_{mq} \Delta P_m - G_{pq} \Delta P - G_{qq} \Delta Q + G_{gqq} \Delta v_{gq} - G_{v2q} \Delta v_2 + G_{gdq} \Delta v_{gd} - G_{v1q} \Delta v_1 \tag{16}$$

The entirety of the transfer functions used in (16) can be written as:

$$\begin{aligned}
 G_{mq} &= \frac{[Q^*P^*L_g^2i_q^*s + Q^*(R_gP^*L_gi_q^* - P^*\omega^*L_g^2i_d^*)]}{\Delta_q} \\
 &\left(\begin{aligned}
 &P^*L_g^2J\omega^*i_q^*s^3 + [(v_d^{*2}L_g + 2P^*R_gL_g)J\omega^*i_q^* + P^*L_g^2i_q^*((P_m^* - P^*)/\omega^*) + Q^*J\omega^*v_d^*L_g]s^2 \\
 &+ \left[\begin{aligned}
 &(R_g^2P^* + P^*\omega^{*2}L_g^2 + v_d^{*2}R_g)i_q^*J\omega^* + (v_d^{*2}L_g + 2P^*R_gL_g)i_q^*((P_m^* - P^*)/\omega^*) + \\
 &Q^*[(P_m^* - P^*)/\omega^*]v_d^*L_g + J\omega^*v_d^*R_g - P^*L_g^2i_q^* \end{aligned} \right]s \\
 &+ (R_g^2P^*i_q^* + i_q^*P^*\omega^{*2}L_g^2 + i_q^*v_d^{*2}R_g)((P_m^* - P^*)/\omega^*) \\
 &+ [(P_m^* - P^*)/\omega^*]v_d^*R_g - R_gP^*L_gi_q^* + P^*\omega^*L_g^2i_d^* \end{aligned} \right) Q^* \\
 G_{pq} &= \frac{\Delta_q}{\Delta_q} \\
 &\left(\begin{aligned}
 &P^*L_g^2J\omega^*s^3 + [(v_d^{*2}L_g + 2P^*R_gL_g)J\omega^* + P^*L_g^2((P_m^* - P^*)/\omega^*)]s^2 \\
 &+ \left[\begin{aligned}
 &(R_g^2P^* + P^*\omega^{*2}L_g^2 + v_d^{*2}R_g)J\omega^* + (v_d^{*2}L_g + 2P^*R_gL_g)((P_m^* - P^*)/\omega^*) \end{aligned} \right]s \\
 &+ (R_g^2P^* + P^*\omega^{*2}L_g^2 + v_d^{*2}R_g)((P_m^* - P^*)/\omega^*) \end{aligned} \right) i_d^* \\
 G_{qq} &= \frac{\Delta_q}{\Delta_q} \\
 G_{gqq} &= \frac{(JP^*\omega^{*2}L_gQ^*s + (P_m^* - P^*)Q^*P^*L_g)}{\Delta_q} \\
 G_{v2q} &= \frac{(JP^*\omega^{*2}L_gQ^*s + (P_m^* - P^*)Q^*P^*L_g)}{\Delta_q} \\
 G_{gdq} &= \frac{(J\omega^*L_gP^*Q^*s^2 + [(P_m^* - P^*)/\omega^*]L_gP^* + J\omega^*R_gP^*)Q^*s + ((P_m^* - P^*)/\omega^*)R_gP^*Q^*}{\Delta_q} \\
 G_{v1q} &= \frac{(J\omega^*L_gP^*Q^*s^2 + [(P_m^* - P^*)/\omega^*]L_gP^* + J\omega^*R_gP^*)Q^*s + ((P_m^* - P^*)/\omega^*)R_gP^*Q^*}{\Delta_q} \\
 \Delta_q &= \left(\begin{aligned}
 &P^*L_g^2J\omega^*s^3 + [(v_d^{*2}L_g + 2P^*R_gL_g)JP^*\omega^* + P^*L_g^2((P_m^* - P^*)/\omega^*)]s^2 \\
 &+ \left[\begin{aligned}
 &(R_g^2P^{*2} + P^{*2}\omega^{*2}L_g^2 + P^*v_d^{*2}R_g)J\omega^* + (v_d^{*2}P^*L_g + 2P^{*2}R_gL_g)((P_m^* - P^*)/\omega^*) \end{aligned} \right]s \\
 &+ (R_g^2P^{*2} + P^{*2}\omega^{*2}L_g^2 + P^*v_d^{*2}R_g)((P_m^* - P^*)/\omega^*) \end{aligned} \right)
 \end{aligned}$$

It can be seen from (15) and (16) that the perturbation part of both the d and q components of the SAPIRC-based converter current can be changed by the mechanical parameters, including the virtual inertia, the reference value of mechanical power, and the virtual mechanical power error. By noticing this role of the mechanical properties, the proposed control technique can be shown as in Figure 2a,b. The proposed control strategy is designed based on Equations (13)–(16), in which the angular frequency error is generated by passing the mechanical power error from a LPF, while two separate PI controllers are considered for the current errors. To further emulate the inherent behaviors of PMSG, both mechanical power and angular frequency errors are involved with the proposed control technique by passing from the related transfer function and relation, as well as a PIR controller, as shown in Figure 2a,b. The considered resonant controller will be defined as follows:

$$[R](s) = \frac{2k_r\omega_c s}{s^2 + 2\omega_c s + \omega_0^2} \tag{17}$$

The coefficients of k_r , ω_c and ω_0 given in Table 1 are chosen in order to minimize the fluctuations of active and reactive power. It can be noted that, observing Figure 2a,b, the resonant controller of (17) is combined with its related PI controller, which is related to the characteristics of PMSG to provide a stable performance for the ultimate control technique.

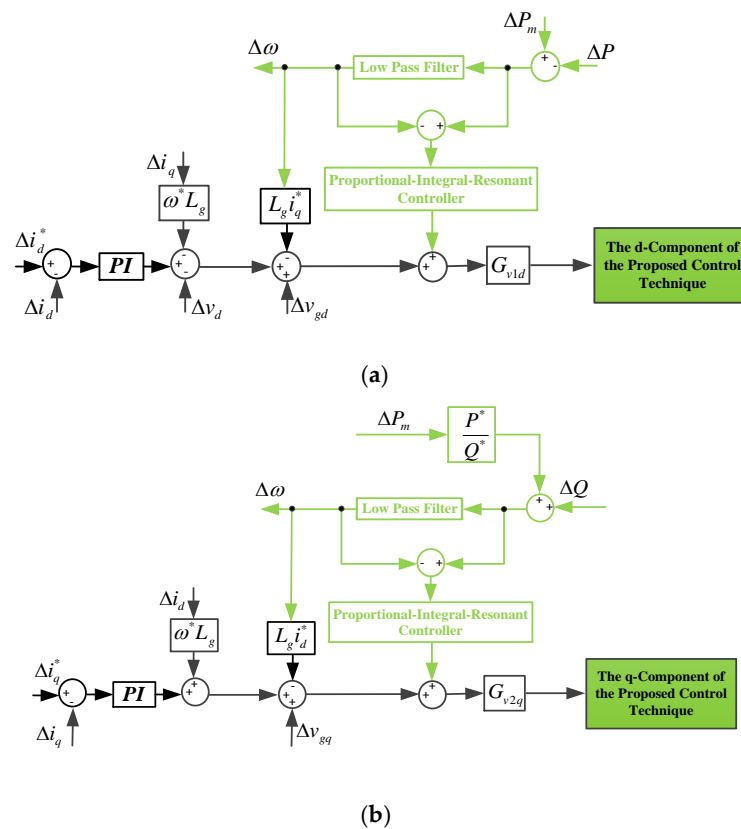


Figure 2. The proposed controller: (a) *d*-component; (b) *q*-component.

Table 1. The parameters and power values considered in simulation section.

Parameters	Values	Parameters	Values
R	0.1 ohm	P_m	$P/0.9$
L	45 mH	Active power of constant load	6 MW
R_g	0.1 ohm	Reactive power of constant load	4 MVAR
L_g	0.1 mH	Active power of the sudden connection	11 MW
Switching frequency	5 kHz	Reactive power of the sudden connection	10 MVAR
Main frequency	50 Hz	Active power of the sudden disconnection	10 MW
DC link voltage	850 V	Reactive power of the sudden disconnection	8 MVAR
k_r	10	$\omega_c = \omega_0/3$	102
Phase grid voltage	220 V	Active power of the sudden disconnection for various resonant factors	12 MW
J	1×10^{-3} s	Reactive power of the sudden disconnection for various resonant factors	11 MVAR

3. Assessment of the Power Converter Currents

In accordance with (15) and (16), the Nyquist diagrams of Δi_d and Δi_q given in Table 1 are shown in Figures 3 and 4, respectively, based on the constant value of the virtual mechanical power error, the *d* component of the grid voltage, and the power converter active and reactive power. In addition to Table 1 for reference and parameter values, other values needed for drawing Figures 3–7 can be stated as $\Delta P_m = 100$ W, $\Delta \omega = 0.1$ Hz, $\Delta v_d = 5$ V and $\Delta v_q = 0$ V. As can be seen from Figure 3, the response of Δi_d is stable, and very low amplitude can also be achieved for this error, which verifies the appropriate performance of the proposed control technique. Taking into account this issue, the lowest value belongs to the variations of ΔP_m , which shows the damped effects of the virtual mechanical power error, as illustrated in Figure 3a. According to Figure 4, Δi_q can achieve stable response under operating conditions. On the other hand, the lowest value for Δi_q is due to the reactive power error as depicted in Figure 4c. Taken together, Figures 3 and 4 verify a stable tracking for the SAPIRC-based power converter.

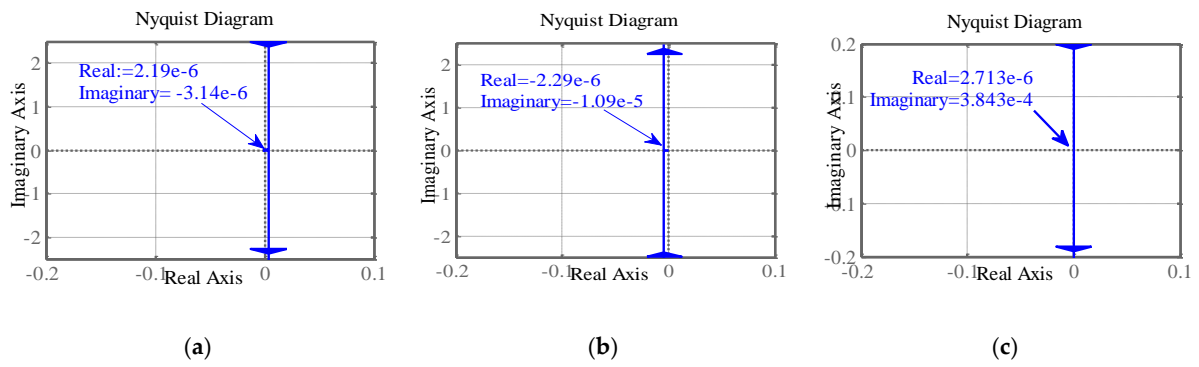


Figure 3. The Nyquist diagram of Δi_d for constant values of: (a) ΔP_m ; (b) ΔP ; (c) Δv_{gd} .

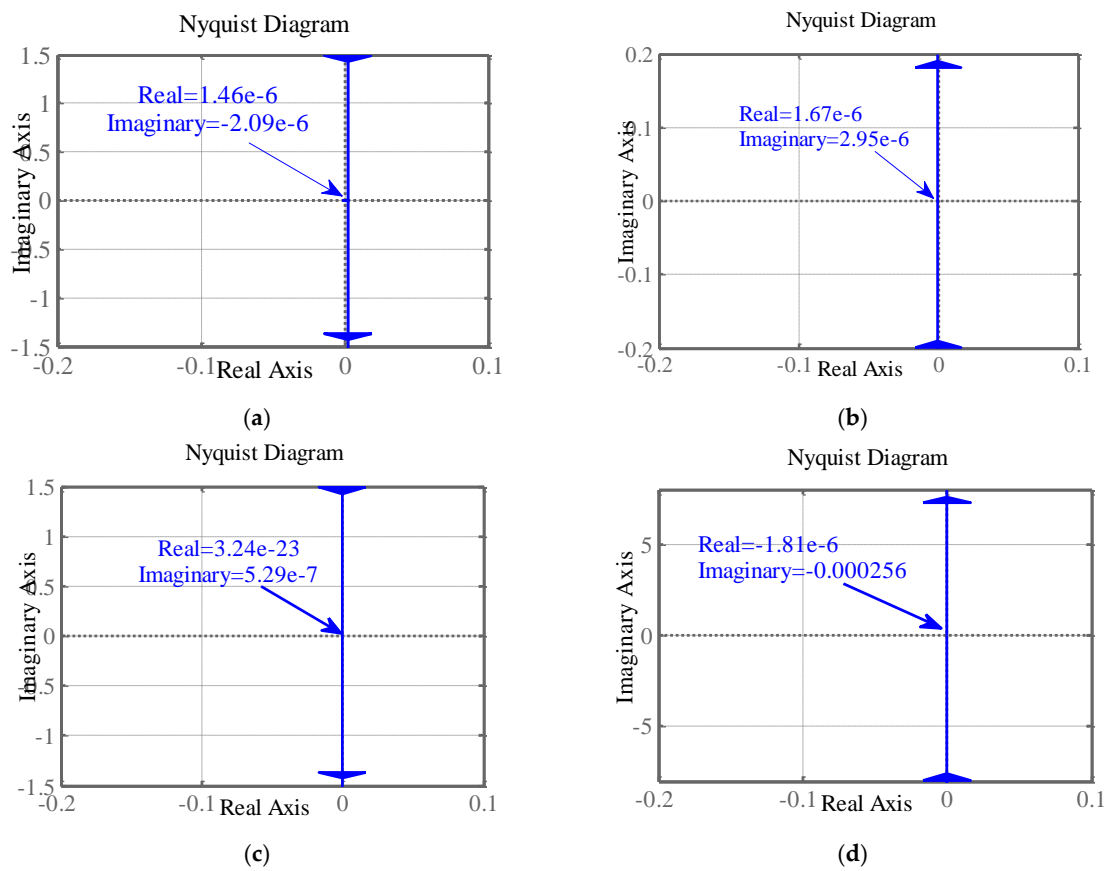


Figure 4. The Nyquist diagram of Δi_q for constant values of: (a) ΔP_m ; (b) ΔP ; (c) ΔQ ; (d) Δv_{gd} .

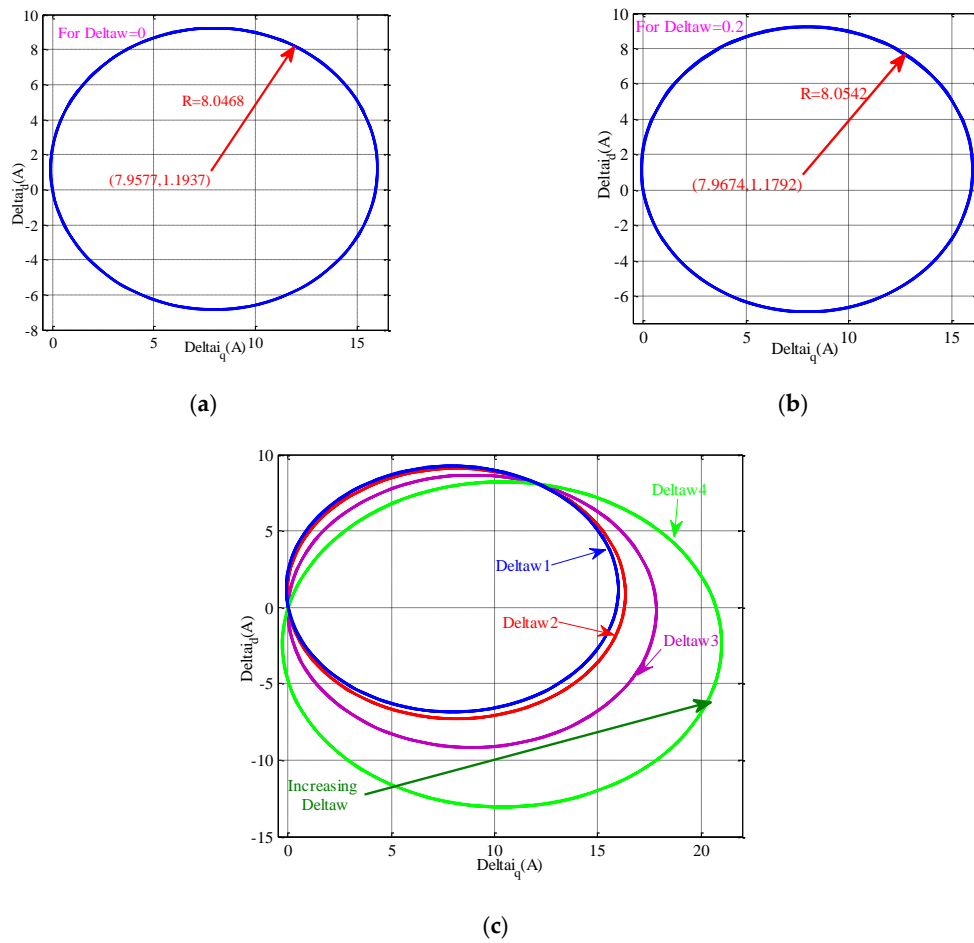


Figure 5. Effects of grid frequency error variation on the current error curve: (a) $\Delta\omega = 0$ Hz; (b) $\Delta\omega = 0.2$ Hz; (c) for various grid frequency errors.

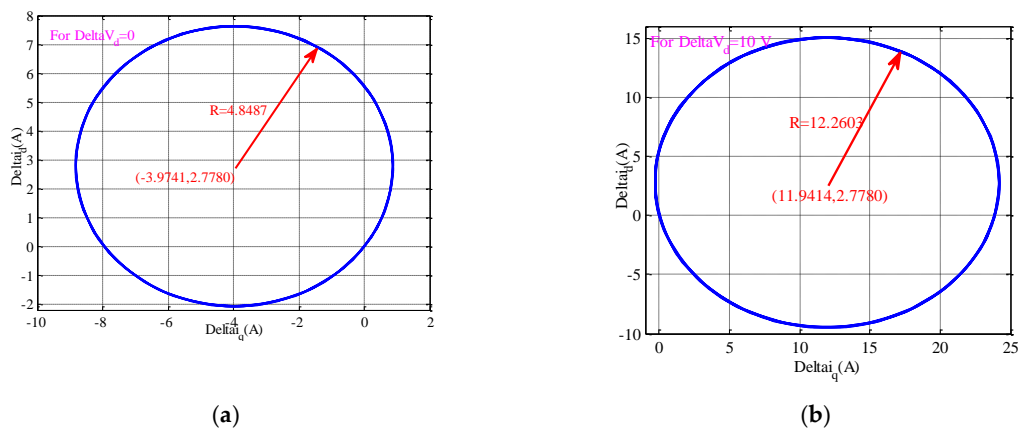
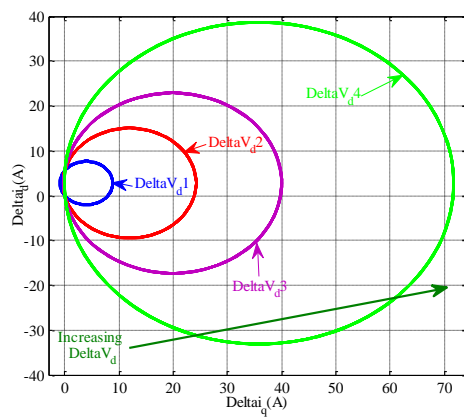
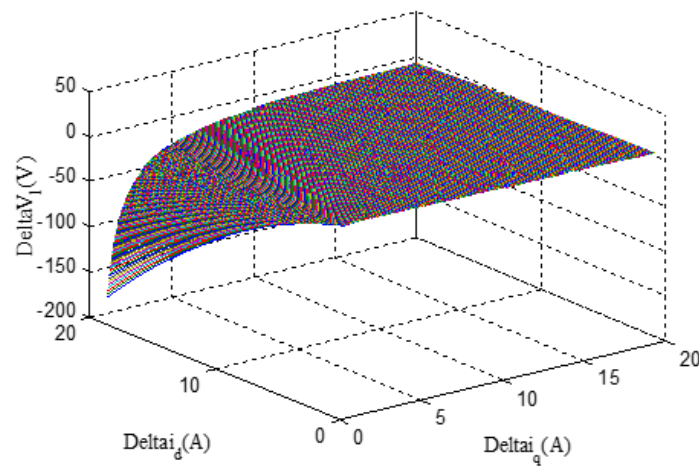


Figure 6. Cont.

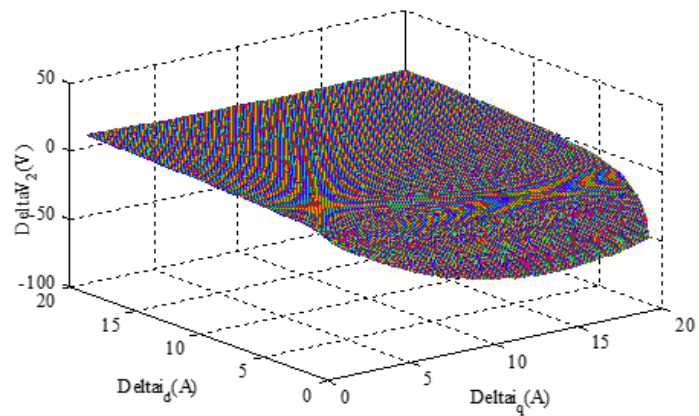


(c)

Figure 6. Effects of the variation of grid voltage magnitude error on the current error curve: (a) $\Delta v_d = 0$ V; (b) $\Delta v_d = 10$ V; (c) for various grid voltage magnitude errors.



(a)



(b)

Figure 7. The current perturbation components effects on: (a) Δv_1 ; (b) Δv_2 .

4. Assessment of the Proposed Current Perturbation Curve (CPC)

In this section, perturbations in both the d and q current components of the SAPIRC-based converter will be influenced by the grid frequency and voltage magnitude alterations. In the first step,

an area based on various operating points for these components will be achieved. By incorporating Equations (6) and (7), (18) can be expressed as:

$$\begin{aligned} & \left(\Delta i_q + \frac{L_g i_q^* \Delta \omega - \Delta(v_{gd} - v_d) + \Delta v_1}{2\omega^* L_g} \right)^2 + \left(\Delta i_d + \frac{L_g i_d^* \Delta \omega + \Delta v_{gq} - \Delta v_2}{2\omega^* L_g} \right)^2 = \\ & \left(\frac{L_g i_q^* \Delta \omega - \Delta(v_{gd} - v_d) + \Delta v_1}{2\omega^* L_g} \right)^2 + \left(\frac{L_g i_d^* \Delta \omega + \Delta v_{gq} - \Delta v_2}{2\omega^* L_g} \right)^2 \end{aligned} \quad (18)$$

Equation (18) is the perturbation curve of SAPIRC, which is shown in Figure 5. This figure verifies how much the variations of grid angular frequency error can influence the alteration zone of Δi_d and Δi_q . By using the system parameters given in Table 1, it is clearly specified in Figure 5a,b that there is a slight difference between the center coordinates and radius of the two generated CPCs due to the two acceptable minimum and maximum values of error in the grid angular frequency. Apart from the grid angular frequency error, choosing the desired value of zero and also the allowable maximum value for the grid voltage magnitude will lead to Figure 6a,b, respectively, in which a large difference between the achieved center coordinates and radius values is depicted. These results confirm that the variations of grid voltage magnitude can impact the current perturbation components much more than the angular frequency error alterations. On the other hand, increasing the grid angular frequency error can expand the operating region of the current perturbation curve, according to Figure 5c. This expansion is more visible for much larger values of $\Delta \omega_3$ and $\Delta \omega_4$. For variations in grid voltage magnitude error, the noticeable expansion of the CPC starts from the first step of the increasing process, as shown in Figure 6c. Based on Figure 6c, the spreading out of the CPC due to the increment in error of the grid voltage magnitude takes place in such a way that sometimes the perturbation values of the SAPIRC-based converter current are not acceptable for continuing operation of the proposed model.

5. Effects of the Current Perturbation Components on the Load-Based Voltage.

The voltages of Δv_1 and Δv_2 that are due to the load current errors can be affected by the current perturbation components of Δi_d and Δi_q . In order to appropriately supply a load, very low values for the load current errors are required, which subsequently leads to a significant decrement in both Δv_1 and Δv_2 . By using (6) and (7), the following equation can be expressed:

$$\begin{aligned} F(\Delta i_q, \Delta i_d, \Delta v_1, \Delta v_2) &= \Delta i_q^2 + \Delta i_d^2 + \left(\frac{\Delta v_1}{\omega^* L_g} \right) \Delta i_q - \left(\frac{\Delta v_2}{\omega^* L_g} \right) \Delta i_d \\ &+ \left(\frac{L_g i_q^* \Delta \omega - \Delta(v_{gd} - v_d)}{\omega^* L_g} \right) \Delta i_q + \left(\frac{L_g i_d^* \Delta \omega + \Delta v_{gq}}{\omega^* L_g} \right) \Delta i_d = 0 \end{aligned} \quad (19)$$

The load-based voltages are considered separately to assess the effects of the current perturbation components. Initially, by assuming $\Delta v_2 = 0$ and then $\Delta v_1 = 0$ in (19), the following relationships can be derived for Δv_1 and Δv_2 , respectively, as:

$$\begin{aligned} F(\Delta i_q, \Delta i_d, \Delta v_1, 0)_{\Delta v_2=0} &= F_1 = 0 \Rightarrow \\ \Delta v_1 &= - \frac{\Delta i_q^2 + \Delta i_d^2 + \left(\frac{L_g i_q^* \Delta \omega - \Delta(v_{gd} - v_d)}{\omega^* L_g} \right) \Delta i_q + \left(\frac{L_g i_d^* \Delta \omega + \Delta v_{gq}}{\omega^* L_g} \right) \Delta i_d}{\left(\frac{\Delta i_q}{\omega^* L_g} \right)} \end{aligned} \quad (20)$$

$$\begin{aligned} F(\Delta i_q, \Delta i_d, 0, \Delta v_2)_{\Delta v_1=0} &= F_2 = 0 \Rightarrow \\ \Delta v_2 &= \frac{\Delta i_q^2 + \Delta i_d^2 + \left(\frac{L_g i_q^* \Delta \omega - \Delta(v_{gd} - v_d)}{\omega^* L_g} \right) \Delta i_q + \left(\frac{L_g i_d^* \Delta \omega + \Delta v_{gq}}{\omega^* L_g} \right) \Delta i_d}{\left(\frac{\Delta i_d}{\omega^* L_g} \right)} \end{aligned} \quad (21)$$

Two three-dimensional diagrams based on (20) and (21) are depicted in Figure 7a,b, respectively. It can be seen from Figure 7a,b that the zero values of the current perturbation components are able to maintain the load-based voltages at their desired value of zero. In addition to very low values of

Δi_d and Δi_q , another desirable case for Δv_1 is achieved with high values of Δi_q and small values of Δi_d , which causes the load-based voltages of Δv_1 to approach zero, as illustrated in Figure 7a. Inversely, the large and small values for Δi_d and Δi_q , respectively, lead to a dramatic increment of Δv_1 , as shown in Figure 7a. On the other hand, as can be seen from Figure 7b, an inverse progression happens for Δv_2 in comparison with Δv_1 . This means that large and small values of Δi_q and Δi_d , respectively, represent an undesirable case for Δv_2 . According to Figure 7b, increasing Δi_d and decreasing Δi_q can lead to obtaining an approximately zero value for Δv_2 . The aforementioned assessments of the load-based voltages variations result in reaching a point at which the correct operation of the SAPIRC for supplying the required currents of the considered loads can be only obtained when Δi_d and Δi_q approach very low or zero values. Thus, it is worth mentioning that increasing one of the two current perturbation components will surely lead to unsuitable performance of the SAPIRC, leading to an unstable power grid.

6. Results and Discussion

The ability of the proposed control technique is evaluated in this section. To present a suitable assessment, the effects of the integration of large-scale RERs, as well as the effects of the resonant factor variations on the proposed control technique are investigated. The simulation parameters are given in Table 1. The general structures of all considered scenarios under simulation are illustrated in Figure 8a,b.

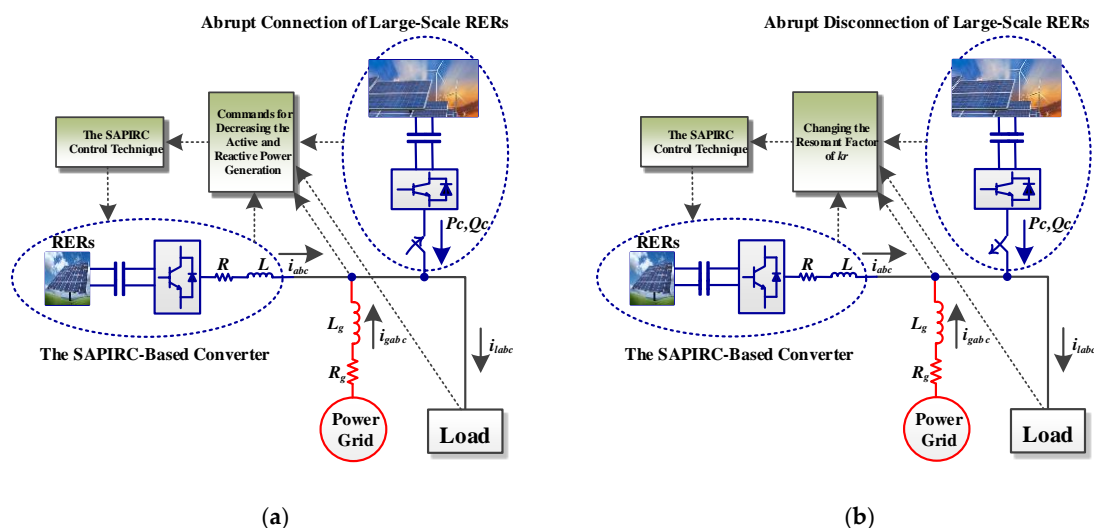


Figure 8. Operation of the SAPIRC-based converter under high penetration of RERs: (a) under a sudden connection, and (b) different values of the resonant factor under sudden disconnection.

A. Effects of the Sudden Connection of Large-Scale RERs

Figure 8a shows the conditions considered in this sub-section. Initially, the power grid and the power converter supply the grid-connected load. Then, at $t = 0.1$ s, the connection of the large-scale RERs takes place and an additional active and reactive power of $11 \text{ MW} + j10 \text{ MVAR}$ is injected to the power grid. After that, the proposed control technique-based converter is implemented at $t = 0.2$ s to support the power grid in reaching stable operating conditions. In the interval $(0, 0.1)$ s, because of the need for the power grid to cover part of the load demand, the grid voltage magnitude is below its desired value and also the grid frequency experiences some fluctuations, as depicted in Figure 9. Under these conditions, the grid current will be as shown in Figure 9. Since the grid voltage magnitude and frequency are not equal to their reference values, the power converter generates its active and reactive power with a small error, as illustrated in Figure 9. After the abrupt integration of the large-scale RERs into the power grid at $t = 0.2$ s, the grid voltage magnitude rises, and the grid

frequency decreases, as shown in Figure 9. These variations are due to the injection of additional active and reactive power into the power grid, whereby the grid current increases, as shown in Figure 9. As can be seen, the alterations of the grid voltage magnitude and frequency will lead to higher error in the active and reactive power injection by the power converter at time interval (0.1, 0.2 s). To amend the grid voltage magnitude and frequency, the additional injected active and reactive power should be compensated. Thus, by noticing the amount of the additional injected power, the power converter operates at $t = 0.2$ s to decrease its active and reactive power injection. Based on Figure 9, after an acceptable transient response, the grid voltage magnitude and frequency appropriately follow their desired values. Also, in contrast to the uncompensated state, as predicted, the grid currents will decrease.

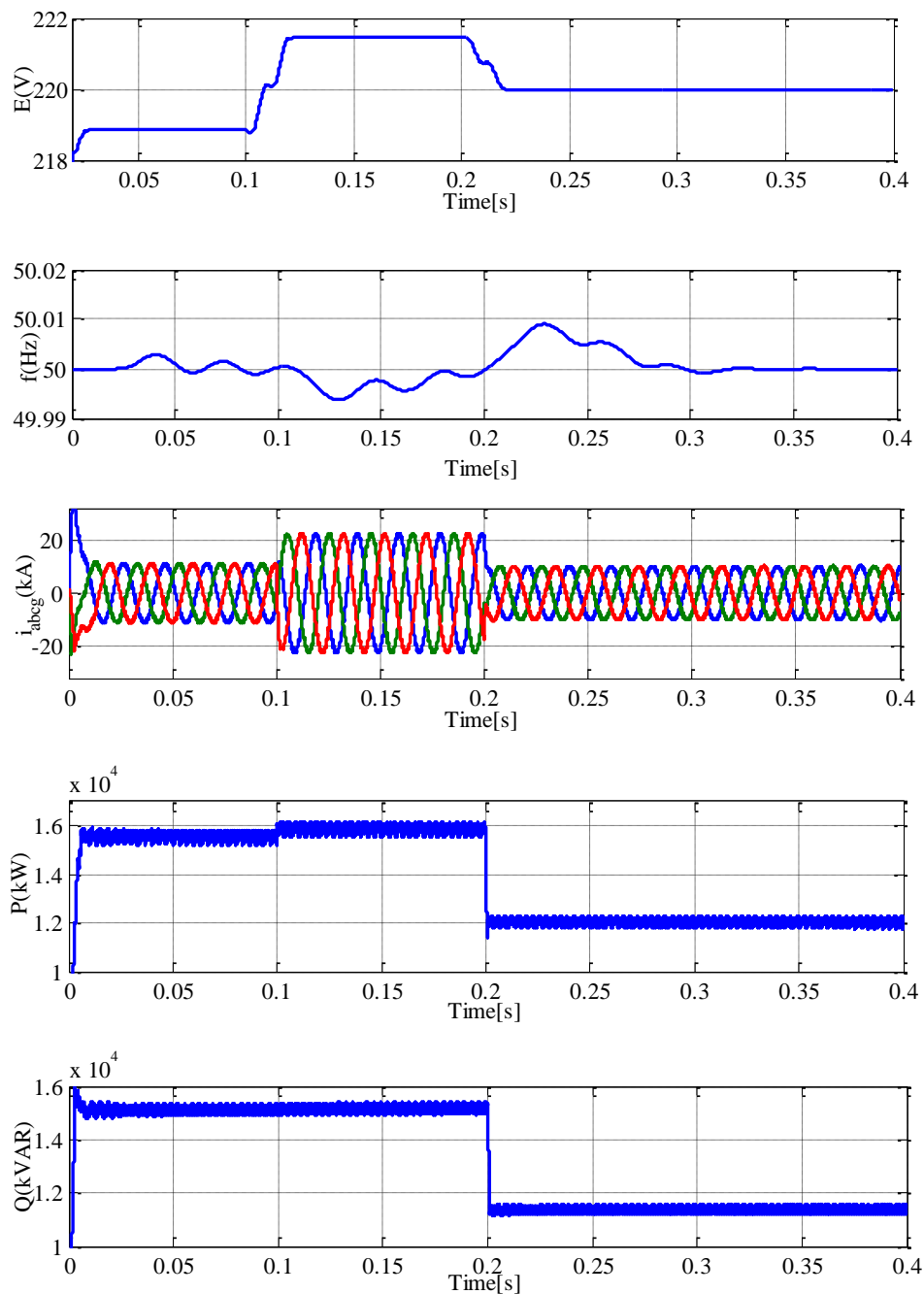


Figure 9. The grid voltage magnitude and frequency, the grid currents, and the active and reactive power of SAPIRC-based converter under a sudden connection of large-scale RERs.

B. Assessment of the Effects of Resonant Factor Variations

In this sub-section, how much the resonant factor can impact the performance of the proposed control technique is investigated, as shown in Figure 8b. The considered scenario is the disconnection of the large-scale RERs, which happens at $t = 0.1$ s, and the power converter compensates this disconnection at $t = 0.25$ s. Figure 10 demonstrates the active and reactive power of the SAPIRC-based converter, the grid voltage magnitude, and the grid frequency under small (k_{r1}), large (k_{r2}) and very large (k_{r3}) values of the resonant factor. These values are 1×10^1 , 1×10^3 and 1×10^5 for k_{r1} , k_{r2} and k_{r3} , respectively. For the case of k_{r1} , all the considered state variables maintain their stable operation in both steady-state and dynamic operating conditions, as depicted in Figure 10. As can be seen from Figure 10, the reactive power becomes unstable faster than the active power for the case of k_{r2} . However, active and reactive powers in both power converters fluctuate greatly after $t = 0.1$ s when considering the resonant factor of k_{r2} . It should be noted that the reactive power fluctuations happen on the routes of its reference value, as shown in Figure 10b. Also, except for the time interval (0, 0.1 s), both the grid voltage magnitude and frequency exhibit unstable behavior for the case of k_{r2} , as demonstrated in Figure 10c,d, respectively. In contrast with k_{r1} , all of the state variables are completely disturbed by choosing the very large value of k_{r3} . Based on Figure 10, the worst case belongs to the active power of the power converter, which oscillates with a very wide amplitude of fluctuations.

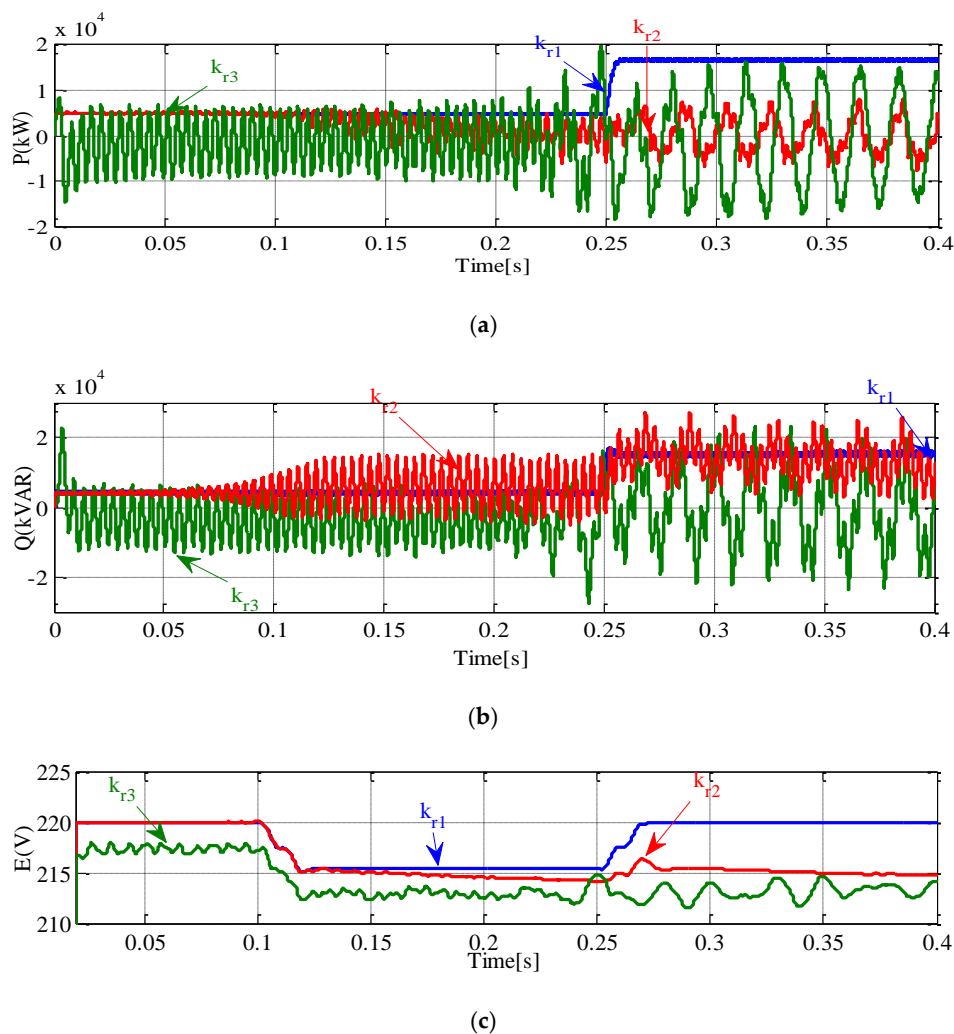


Figure 10. Cont.

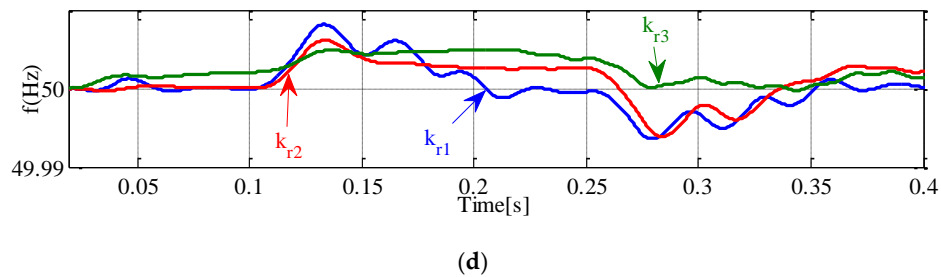


Figure 10. Evaluation of the resonant factor variations: (a) active power of the SAPIRC-based converter; (b) reactive power of the SAPIRC-based converter; (c) the grid voltage magnitude; (d) the grid frequency.

7. Conclusions

A synchronous resonant control technique has been presented in this paper to address power grid instability problems due to the high penetration of renewable energy resources. After applying small signal linearization to a dynamic model with state variables, i.e., the grid parameters, the load-based voltages, and currents of the proposed control-based converter, the linearized relationships based on the inherent features of the PMSG and the apparent power of the interfaced converter were utilized to add a new functionality to the control loop of the interfaced converter based on the behavior of the synchronous generator. As a contribution of the proposed control strategy, a comprehensive relationship between interfaced converter model and PMSG inherent swing equations has been established. Also, the impacts of the errors of virtual mechanical power, the d-axis of the grid voltage, and the active and reactive power of the interfaced converter were applied to the converter currents errors. To further analyze the power grid frequency and voltage magnitude errors, a CPC was introduced. Moreover, the appropriate operation for supplying the grid-connected loads was accurately assessed through the perturbation components variation analysis of the proposed controller-based converter currents. Simulation results confirmed the ability of the proposed control technique to guarantee stable operation of the power grid under high penetration of renewable energy resources.

Author Contributions: All authors worked on this manuscript together and all authors have read and approved the final manuscript.

Funding: This research was funded by FEDER funds through COMPETE 2020, Portuguese funds through FCT, under Projects SAICT-PAC/0004/2015-POCI-01-0145-FEDER-016434, POCI-01-0145-FEDER-006961, UID/EEA/50014/2013, UID/CEC/50021/2013, UID/EMS/00151/2013, 02/SAICT/2017-POCI-01-0145-FEDER-029803, and the EU 7th Framework Programme FP7/2007-2013 under GA no. 309048.

Acknowledgments: J.P.S. Catalão acknowledges the support by FEDER funds through COMPETE 2020 and by Portuguese funds through FCT, under Projects SAICT-PAC/0004/2015—POCI-01-0145-FEDER-016434, POCI-01-0145-FEDER-006961, UID/EEA/50014/2013, UID/CEC/50021/2013, UID/EMS/00151/2013, and 02/SAICT/2017—POCI-01-0145-FEDER-029803, and also funding from the EU 7th Framework Programme FP7/2007-2013 under GA no. 309048.

Conflicts of Interest: The authors declare no conflict of interest.

Nomenclature

Parameters

R_g	Grid Resistance
L_g	Grid Inductance
J	Moment of Inertia

Variables

i_{dq}	Converter Currents
i_{ldq}	Load Currents
i_{gdq}	Grid Currents

Δi_{dq}	Perturbation Components of i_{dq}
Δi_{ldq}	Perturbation Components of i_{ldq}
Δi_{gdq}	Perturbation Components of i_{gdq}
v_{dq}	Converter Voltage Magnitudes
v_{gdq}	Grid Voltage Magnitudes
v_{12}	Load-Based Voltages
Δv_{dq}	Perturbation Components of v_{dq}
Δv_{12}	Perturbation Components of v_{12}
Δv_{gdq}	Perturbation Components of v_{gdq}
P_m	Mechanical Power
P, Q, S	Active, Reactive and Apparent Power of SAPIRC-Based Converter
ω	Grid Angular Frequency
$\Delta P, \Delta Q$	Perturbation Components of P and Q
ΔP_m	Perturbation Components of P_m
$\Delta \omega$	Perturbation Components of ω
i_{dq}^*	Reference Values of i_{dq}
v_{dq}^*	Reference Values of v_{dq}
P^*, Q^*	Reference Values of P, Q
P_m^*	Reference Values of P_m
ω^*	Reference Values of ω
Δi_{dq}^*	Reference Values of Δi_{dq}
k_{pdq}, k_{idq}	PI Controller Coefficients
k_r	Resonant Factor
ω_0, ω_c	Frequencies of Resonant Controller
Abbreviation	
SAPIRC	Synchronous Active Proportional Integral Resonant Controller
PMSG	Permanent Magnet Synchronous Generator
CPC	Current Perturbation Curve
RERs	Renewable Energy Resources
LPF	Low Pass Filter
PI	Proportional Integral
PV	Photovoltaic

References

1. Valenciaga, F.; Puleston, P.F.; Battaiotto, P.E.; Mantz, R.J. Passivity/sliding mode control of a stand-alone hybrid generation system. *IEE Proc.—Control Theory Appl.* **2000**, *147*, 680–686. [[CrossRef](#)]
2. Hosseinzadeh, M.; Salmasi, F.R. Power management of an isolated hybrid AC/DC micro-grid with fuzzy control of battery banks. *IET Renew. Power Gener.* **2015**, *9*, 484–493. [[CrossRef](#)]
3. Hosseinzadeh, M.; Salmasi, F.R. Robust optimal power management system for a hybrid AC/DC micro-grid. *IEEE Trans. Sustain. Energy* **2015**, *6*, 675–687. [[CrossRef](#)]
4. Hosseinzadeh, M.; Salmasi, F.R. Analysis and detection of a wind system failure in a micro-grid. *J. Renew. Sustain. Energy* **2016**, *8*. [[CrossRef](#)]
5. Mehrasa, M.; Pouresmaeil, E.; Zabihi, S.; Rodrigues, E.M.G.; Catalao, J.P.S. A control strategy for the stable operation of shunt active power filters in power grids. *Energy* **2016**, *96*, 325–334. [[CrossRef](#)]
6. Pouresmaeil, E.; Mehrasa, M.; Shokridehaki, M.A.; Rodrigues, E.M.G.; Catalao, J.P.S. Control and stability analysis of interfaced converter in distributed generation technology. In Proceedings of the IEEE EUROCON 2015—International Conference on Computer as a Tool (EUROCON), Salamanca, Spain, 8–11 September 2015; pp. 1–6.
7. Pouresmaeil, E.; Mehrasa, M.; Erdinc, O.; Catalao, J.P.S. A control algorithm for the stable operation of interfaced converters in microgrid systems. In Proceedings of the IEEE PES Innovative Smart Grid Technologies, Istanbul, Turkey, 12–15 October 2014; pp. 1–6.

8. Mei, J.; Xiao, B.; Shen, K.; Tolbert, L.M.; Zheng, J.Y. Modular multilevel inverter with new modulation method and its application to photovoltaic grid-connected generator. *IEEE Trans. Power Electron.* **2013**, *28*, 5063–5073. [[CrossRef](#)]
9. Pouresmaeil, E.; Mehraza, M.; Shokridehaki, M.A.; Rodrigues, E.M.G.; Catalao, J.P.S. Control of modular multilevel converters for integration of distributed generation sources into the power grid. In Proceedings of the IEEE International Conference on Smart Energy Grid Engineering (SEGE), Oshawa, ON, Canada, 17–19 August 2015; pp. 1–6.
10. Hasanzadeh, A.; Edrington, C.S.; Stroupe, N.; Bevis, T. Real-time emulation of a high-speed microturbine permanent-magnet synchronous generator using multiplatform hardware-in-the-loop realization. *IEEE Trans. Ind. Electron.* **2014**, *61*, 3109–3118. [[CrossRef](#)]
11. Griffo, A.; Drury, D. Hardware in the loop emulation of synchronous generators for aircraft power systems. *Electr. Syst. Aircr. Railw. Ship Propuls. (ESARS)* **2012**. [[CrossRef](#)]
12. Valencia, F.; Puleston, P.F. Variable structure control of a wind energy conversion system based on a brushless doubly fed reluctance generator. *IEEE Trans. Energy Convers.* **2007**, *22*, 499–506. [[CrossRef](#)]
13. Valencia, F.; Puleston, P.F.; Battaiotto, P.E. Power control of a photovoltaic array in a hybrid electric generation system using sliding mode techniques. *IEE Proc. Control Theory Appl.* **2001**, *148*, 448–455. [[CrossRef](#)]
14. Pradhan, R.; Subudhi, B. Double integral sliding mode MPPT control of a photovoltaic system. *IEEE Trans. Control Syst. Technol.* **2016**, *24*, 285–292. [[CrossRef](#)]
15. Hosseinzadeh, M.; Salmasi, F.R. Determination of maximum solar power under shading and converter faults—A prerequisite for failure-tolerant power management systems. *Simul. Model. Pract. Theory* **2016**, *62*, 14–30. [[CrossRef](#)]
16. Torres, M.A.; Lopes, L.A.; Moran, L.A.; Espinoza, J.R. Self-tuning virtual synchronous machine: A control strategy for energy storage systems to support dynamic frequency control. *IEEE Trans. Energy Convers* **2014**, *29*, 833–840. [[CrossRef](#)]
17. D’Arco, S.; Suul, J.A.; Fosso, O.B. A virtual synchronous machine implementation for distributed control of power converters in smart grids. *Electric Power Syst Res.* **2015**, *122*, 180–197. [[CrossRef](#)]
18. Sarkar, M.N.I.; Meegahapola, L.G.; Datta, M. Reactive power management in renewable rich power grids: A review of grid-codes, renewable generators, support devices, control strategies and optimization algorithms. *IEEE Access* **2018**, *6*, 41458–41489. [[CrossRef](#)]
19. Ou, T.C.; Hong, C.M. Dynamic operation and control of microgrid hybrid power systems. *Energy* **2014**, *66*, 314–323. [[CrossRef](#)]
20. Hong, C.M.; Ou, T.C.; Lu, K.H. Development of intelligent MPPT (maximum power point tracking) control for a grid-connected hybrid power generation system. *Energy* **2013**, *50*, 270–279. [[CrossRef](#)]
21. Lin, W.M.; Hong, C.M.; Ou, T.C.; Chiu, T.M. Hybrid intelligent control of PMSG wind generation system using pitch angle control with RBFN. *Energy Convers. Manag.* **2011**, *52*, 1244–1251. [[CrossRef](#)]
22. Ou, T.C.; Lu, K.H.; Huang, C.J. Improvement of transient stability in a hybrid power multi-system using a designed NIDC (Novel Intelligent Damping Controller). *Energies* **2017**, *10*, 488. [[CrossRef](#)]
23. Ou, T.C. A novel unsymmetrical faults analysis for microgrid distribution systems. *Int. J. Electr. Power Energy Syst.* **2012**, *43*, 1017–1024. [[CrossRef](#)]
24. Ou, T.C. Ground fault current analysis with a direct building algorithm for microgrid distribution. *Int. J. Electr. Power Energy Syst.* **2013**, *53*, 867–875. [[CrossRef](#)]
25. Lyu, X.; Zhao, J.; Jia, Y.; Xu, Z.; Wong, K.P. Coordinated control strategies of PMSG-based wind turbine for smoothing power fluctuations. *IEEE Trans. Power Syst.* **2018**. [[CrossRef](#)]
26. Mendis, N.; Muttaqi, K.M.; Perera, S. Management of battery-supercapacitor hybrid energy storage and synchronous condenser for isolated operation of PMSG based variable-speed wind turbine generating systems. *IEEE Trans. Smart Grid* **2014**, *5*, 944–953. [[CrossRef](#)]
27. Li, M.; Wang, Y.; Xu, N.; Liu, Y.; Wang, W.; Wang, H.; Lei, W. A novel virtual synchronous generator control strategy based on improved swing equation emulating and power decoupling method. In Proceedings of the 2016 IEEE Energy Conversion Congress and Exposition (ECCE), Milwaukee, WI, USA, 18–22 September 2016; pp. 1–6.

28. Mehra, M.; Gordina, R.; Pouresmaeil, E.; Vechiu, I.; Rodrigues, R.L.; Catalao, J.P.S. Synchronous active proportional resonant-based control technique for high penetration of distributed generation units into power grids. In Proceedings of the 2017 IEEE PES Innovative Smart Grid Technologies Conference Europe (ISGT-Europe), Torino, Italy, 26–29 September 2017. [[CrossRef](#)]
29. Pouresmaeil, E.; Mehra, M.; Gordina, R.; Vechiu, I.; Rodrigues, R.L.; Catalao, J.P.S. Double synchronous controller for integration of large-scale renewable energy sources into a low-inertia power grid. In Proceedings of the 2017 IEEE PES Innovative Smart Grid Technologies Conference Europe (ISGT-Europe), Torino, Italy, 26–29 September 2017. [[CrossRef](#)]
30. Alipoor, J.; Miura, Y.; Ise, T. Stability assessment and optimization methods for microgrid with multiple VSG units. *IEEE Trans. Smart Grid* **2016**, *9*, 1462–1471. [[CrossRef](#)]
31. Hou, X.; Han, H.; Zhong, C.; Yuan, W.; Yi, M.; Chen, Y. Improvement of transient stability in inverter-based AC microgrid via adaptive virtual inertia. In Proceedings of the 2016 IEEE Energy Conversion Congress and Exposition (ECCE), Milwaukee, WI, USA, 18–22 September 2016; pp. 1–6. [[CrossRef](#)]
32. Chamana, M.; Chowdhury, B.H.; Jahanbakhsh, F. Distributed control of voltage regulating devices in the presence of high PV penetration to mitigate ramp-rate issues. *IEEE Trans. Smart Grid* **2018**, *9*, 1086–1095. [[CrossRef](#)]
33. Arricibita, D.; Sanchis, P.; Marroyo, L. Virtual synchronous generators classification and common trends. In Proceedings of the IECON 2016—42nd Annual Conference of the IEEE Industrial Electronics Society, Florence, Italy, 23–26 October 2016; pp. 2433–2438. [[CrossRef](#)]
34. Zhong, Q.C.; Weiss, G. Synchronverters: inverters that mimic synchronous generators. *IEEE Trans. Ind. Electron.* **2011**, *58*, 1259–1267. [[CrossRef](#)]
35. Tan, S.; Lv, Q.; Geng, H.; Yang, G. An equivalent synchronous generator model for current-controlled voltage source converters considering the dynamic of phase-locked-loop. In Proceedings of the IECON 2016—42nd Annual Conference of the IEEE Industrial Electronics Society, Florence, Italy, 23–26 October 2016; pp. 2235–2240. [[CrossRef](#)]
36. Guan, M.; Pan, W.; Zhang, J.; Hao, Q.; Cheng, J.; Zheng, X. Synchronous generator emulation control strategy for voltage source converter (VSC) stations. *IEEE Trans. Power Syst.* **2015**, *30*, 3093–3101. [[CrossRef](#)]
37. Anzalchi, A.; MalekPour, M.; Sarwat, A. A combinatorial approach for addressing intermittency and providing inertial response in a grid-connected photovoltaic system. In Proceedings of the 2016 IEEE Power and Energy Society General Meeting (PESGM), Boston, MA, USA, 17–21 July 2016; pp. 1–5. [[CrossRef](#)]
38. Arco, S.D.; Suul, J.A. Equivalence of virtual synchronous machines and frequency-droops for converter-based microgrids. *IEEE Trans. Smart Grid* **2014**, *5*, 394–395. [[CrossRef](#)]
39. Laudahn, S.; Seidel, J.; Engel, B.; Bülo, T.; Premm, D. Substitution of synchronous generator based instantaneous frequency control utilizing inverter-coupled DER. In Proceedings of the 2016 IEEE 7th International Symposium on Power Electronics for Distributed Generation Systems (PEDG), Vancouver, BC, Canada, 27–30 June 2016; pp. 1–6. [[CrossRef](#)]

